EXPERIMENTAL AND COMPUTATIONAL STUDIES OF CROSSING-SHOCK-WAVE / TURBULENT-BOUNDARY-LAYER INTERACTIONS

A.A. ZHELTOVODOV, A.I. MAKSIMOV
Institute of Theoretical and Applied Mechanics SB RAS, Novosibirsk 630090, Russia
e-mail: zhelt@itam.nsc.ru

E. SCHÜLEIN
German Aerospace Center DLR, Institute of Fluid Mechanics, Goettingen, Germany
e-mail: Erich.Schuelein@dlr.de

D.D. KNIGHT
Rutgers University, Piscataway, New Jersey, USA
e-mail: ddknight@rci.rutgers.edu

F. THIVET
ONERA, Centre de Toulouse, Toulouse, France
e-mail: Frederic.Thivet@onecert.fr

D.V. GAITONDE, J.D. SCHMISSEUR
Computational Sciences Branch Air Vehicle Directorate, Air Force Research Laboratory Wright-Patterson AFB, USA
e-mail: datta@vaa.wpafb.af.mil; schmisjd@vaa.wpafb.af.mil

The regimes and physical features of 3-D symmetric and asymmetric crossing-shock-wave / turbulent-boundary-layer interaction in the vicinity of two fins mounted on a flat plate are analyzed at the Mach number range $M_\infty = 4$ and 5. The possibilities of numerical modeling of the flowfield structure, surface pressure and heat transfer distributions on the basis of the Reynolds averaged three-dimensional time-depended Navier – Stokes equations (RANS) and different turbulence models are demonstrated. The perspectives of the computations improvement on a basis of properties discovered in the experiments are discussed.

Introduction

Experimental study and numerical modeling of crossing-shock-wave/turbulent boundary layer interactions (CSWTBLI) are of critical importance for development of efficient air-breathing propulsion systems for high speed flight (Fig. 1, *a*). These complex three-dimensional (3-D) interactions generally degrades the flowfield quality in proposed promising scramjet designs. They are generally at the origin of important losses in the inlet efficiency as well as often lead to the concentration of high heat fluxes in some regions of the inlet walls, which can cause serious damages. Such interactions also may become strong enough to cause the unstart of the inlet. Development of advanced numerical methods require a comprehensive understanding of the physics of CSWTBLI by examples of simplified canonical configurations. Two symmetric ($\beta_1 = \beta_2$) or asymmetric ($\beta_1 \neq \beta_2$) sharp vertical fins mounted on a flat plate (Fig. 1, *b*) are among such configurations actively studied the last decade.

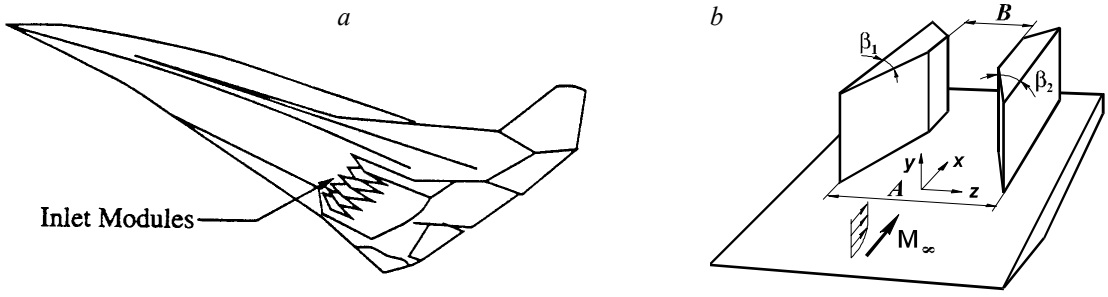

Fig. 1. Hypersonic aircraft with the air-breathing propulsion system (*a*); double-fin test configuration (*b*)

Wide review of theoretical and experimental studies of the CSWTBLI can be found in [1–5]. Significant research efforts have been concentrated on the development and evaluation of turbulence models capable of providing accurate predictions of the flow structure and aerothermodynamic loads on the bottom flat-plate surface. The computed flows generally exhibit good agreement with the experimental data for surface pressure, shock structure and boundary layer profiles of pitot pressure and yaw angle for limited range of the crossing-shock-wave (CSW) strength. However, the accurate prediction of surface heat transfer and skin friction remains a challenging problem. Recent studies [6–10] distinctly demonstrates obvious limitations of various turbulence models to predict correctly different properties of symmetric and asymmetric CSWTBLI for a wide range of CSW strength. They have stimulated new attempts to analyze the possibilities of two-equation k–ω turbulence model for predicting the properties of such flows [11–14].

The objective of the present paper is to present a comprehensive comparison between experimental and last computational data and asses the capability of the popular two-equation k–ω and k–ε turbulence models to predict CSWTBLI as well as suggest new directions of work for improving the agreement between experiment and CFD.

1. Test configurations and experimental methods

The configurations (Fig. 1, *b*) correspond to experiments conducted at the Institute of Theoretical and Applied Mechanics (ITAM) SB RAS, Novosibirsk by Zheltovodov *et al.* [4, 5] in the supersonic wind tunnel T-333 at the flow nominal Mach number M_∞ = 3 and 4 as well as at the German Aerospace Center, Goettingen by Schülein and Zheltovodov [15, 16] in the supersonic/hypersonic Ludwieg-Tube (RWG) at M_∞ = 5. The six possible combinations (symmetric and asymmetric) of two fins of angle 7°, 11°, 15° have been experimentally studied at ITAM. The model is a plate with two symmetrical or asymmetrical mounted fins with sharp leading edges, located at a distance of 210 mm from the plate leading edge. Chamfered fins of length 192 mm and height 100 mm are employed, separated by a minimum distance B = 32 mm in the constant width section (the throat). The throat middle line (TML) forms the x axis. Four of combinations studied at M_∞ = 4 are retained here for the comparison with computations: the 7°×7° (weak symmetric interaction) with the entrance width A = 71.5 mm, 7°×11° (mild asymmetric interaction) with A = 73.6 mm, 15°×15° (strong symmetric interaction) with A = 79.1 mm and 7°×15° (strong asymmetric interaction) with A = 75.4 mm. The total pressure P_0 = 1485 (–5/+13) kPa, and the total temperature T_0 = 260 (±4) K, yeald a Reynolds number close to $88\cdot10^6$ /m for these cases. The measurements consist of surface flow visualization by an oil film technique, pressures and adiabatic temperatures along the TML and three cross sections (marked I, II, III in Figs. 2 and 4) at the bottom wall in adiabatic conditions. The Stanton number is also obtained, using the electric-calorimetry (the heating thin wall) method. The random measurement error and the systematic error due to the heat flux losses for radiation and heat overflow are estimated as being in ±15 %. The boundary layer thickness and momentum thickness are respectively δ_0 = 3.5 mm and θ = 0.128 mm, 14 mm upstream of the fin leading edge section.

The seven basic symmetric combinations of two fins of angle 8°, 12°, 16°, 17°, 17.5°, 18°, 23° have been experimentally studied at the DLR, Institute of Fluid Mechanics at M_∞ = 5 [15, 16]. Only one of them is retained here for the comparison with computations: 23°×23° (very strong symmetric interaction) with A = 307 mm. The fins with the height 100 mm had flat side faces and the minimal width between their trailing edges was B = 100 mm. The stagnation conditions P_0 = 2210 (±10) kPa and T_0 = 427 (±6) K, result in a Reynolds number close to $36.5\cdot10^6$ /m. The wall temperature is T_w = 295 (±6) K. The boundary layer and momentum thickness are δ_0 = 3.8 mm and θ = 0.157 mm at a distance of $6\delta_0$ upstream of the fin leading edges. The measurements consist of the surface flow visualization by an oil film technique, pressure measurements along the TML and some additional longitudinal sections as well as cross sections (x/δ_0 = 22.1; 24.7; 32.6; 40.5; 48.4) downstream of the fin leading edges. The surface reflecting visualization (SRV) method was also used parallel with the surface flow pattern visualization as well as high speed movie to reveal the mean (in time) and instantaneous CSW structures. The Global Interferometer Skin Friction meter (GISF) was applied for the skin friction measurements upstream of the interaction region and preliminary qualitative analysis of its behavior in the 3-D interaction regions. The processing of these preliminary and additional new data have been performed on the next stage of the studies by Schülein on a basis of GISF method developed for the 3-D flows [17]. Together with quantitative C_f data this paper also includes new heat transfer measurements for some of the cases at M = 5.

2. Theoretical models

The computations by Thivet and Knight on a basis of the the Wilcox' k–ω model [18] are performed with the code *GASP*ex [19], which solves the Reynolds Averaged 3-D compressible time depended Navier-Stokes equations (RANS). Details of the theoretical model and computations may be found in [11–14] and are not repeated here. Briefly, the convected fluxes are computed to third-order accuracy using the Roe scheme and a MUSCL reconstruction method with the Min-Mod limiter. The viscous terms are evaluated by second order central differencing. The steady solution is obtained by applying a time-marching method based on the hybrid Approximate Factorization / Relaxation algorithm. The inflow conditions are applied 14 mm upstream of the fin leading edges, as the mean experimental values

supplemented with a computed boundary layer matching the measured θ values. Turbulence is represented using the Wilcox' k–ω model, implemented with the slightly-rough but hydraulically-smooth-surface boundary conditions and the constant turbulent Prandtl number $\mathrm{Pr}_t = 0.9$ [18, 20]. The adiabatic and the isothermal wall solutions provided the heat flux and the Stanton numbers C_h.

A special effort is made to assess the grid-convergence of the computed results and to show how this point may be. In each considered case, three levels of grid refinement are defined. At each level, the longitudinal step size (along x) is constant and equal to 2 mm (about $0.6\delta_0$). The cells of the fine grid (level 1) are merged two by two in both y and z directions to define the medium grid. (level 2). The coarse grid (level 3) is obtained the same way from the medium grid. In the 15°×15° configuration only, a fourth refinement level is defined, namely the very fine grid level (level 0), obtained by dividing the cells of the fine grid in two in both x and y directions. The details of the grid are gathered in Table 1, where Δy_1^+ is the first cell height above the wall.

Table 1. Grid configurations

Grid	Configurations									
	7°×7°			7°×11°			15°×15°			
	Fine	Medium	Coarse	Fine	Medium	Coarse	Very Fine	Fine	Medium	Coarse
N_{cell}	614400	153600	38400	1228800	307200	76800	3993600	998400	249600	62400
Δy_1^+	0.35–0.5	0.75–1.2	1.9–3.5	0.35–1.3	0.75–3.0	1.9–7.0	0.17–1.0	0.35–2.0	0.75–4.0	1.6–8.2

At the top as well as at the outflow boundary, the solutions is extrapolated to first order from interior. In the symmetrical cases, only half a configurations is computed and a second-order symmetrical condition is prescribed on the symmetry plane. On the bottom and side walls, fully turbulent boundary layers are computed, using a no-slip adiabatic or isothermal condition.

The computations by Gaitonde and Schmisseur have been performed on a basis of the full three-dimensional mean compressible Navier – Stokes equations in strong conservation form and mass-averaged variables. Details may be found in [9, 10, 21–23]. Briefly, the inviscid fluxes are evaluated to nominal third-order accuracy with Roe's flux-difference split scheme together with a limiter to enforce monotonicity. Viscous terms are differenced to second-order accuracy in a centered manner. An implicit time-integration scheme, based on the Beam – Warming approach [24], is employed to march the solution to steady state. The effects of turbulence are incorporated through the eddy viscosity μ_t assumption and the turbulent Prandtl number $\mathrm{Pr}_t = 0.90$. The turbulence model used to determine μ_t is based on the k–ε equations [25, 26] with low Reynolds number terms and a compressibility correction. The incoming boundary-layer profile is specified at the indicated positions upstream of the fin leading edges by matching the momentum thickness with two-dimensional calculations. On the symmetry plane, all gradients are set to zero with the exception of the normal velocity which is itself set to zero instead. On the solid surfaces the no-slip boundary condition is invoked, the wall temperature is specified based on experiment and the normal pressure gradient, k and ε are all assumed to be zero. At the outflow and top boundaries, zero-gradient extrapolation boundary conditions are applied.

Table 2. Grid configurations

Configurations	Resolution	
7°×15°		123×88×197
23°×23°	Mesh 1	91×72× 52
23°×23°	Mesh 2	181×143×103
23°×23°	Mesh 3	229×179×129

The grid employed for each simulation is composed of sequential non-uniform Cartesian planes oriented normal to the freestream direction. Gridpoints are clustered to resolve the secondary features of the interior vortical flowfield, with the location of the clustered regions determined from previous experience. For the 7°×15° strong asymmetric interaction case the solution was computed on the grid with 2.13×10^6 points. For the strongest, 23°×23° interaction, the solution was computed with various grid spacing to yield some indication of the degree of mesh independence [7, 9, 23]. A summary of the parameters for each mesh is presented in Table 2 where is indicated the number of grid points in the streamwise, plate-normal and spanwise directions respectively. The finest mesh, Mesh 3, has about twice as many points as Mesh 2 and consists of 5.3×10^6 mesh points. Convergence of the solution is determined from monitoring the global norm, surface pressure and skin friction coefficients.

3. Comparison of computations with experiment

The experimental topological schemes derived from the oil-flow visualization (Fig. 2, *a-c*, left column a compared with the skin-friction line patterns computed on a basis standard Wilcox's k-ω model (WI) on the bottom plate (Fig. 2, *d–f*). The figures in the right column of Fig.2 are built after the numerical solutions obtained on a fine level

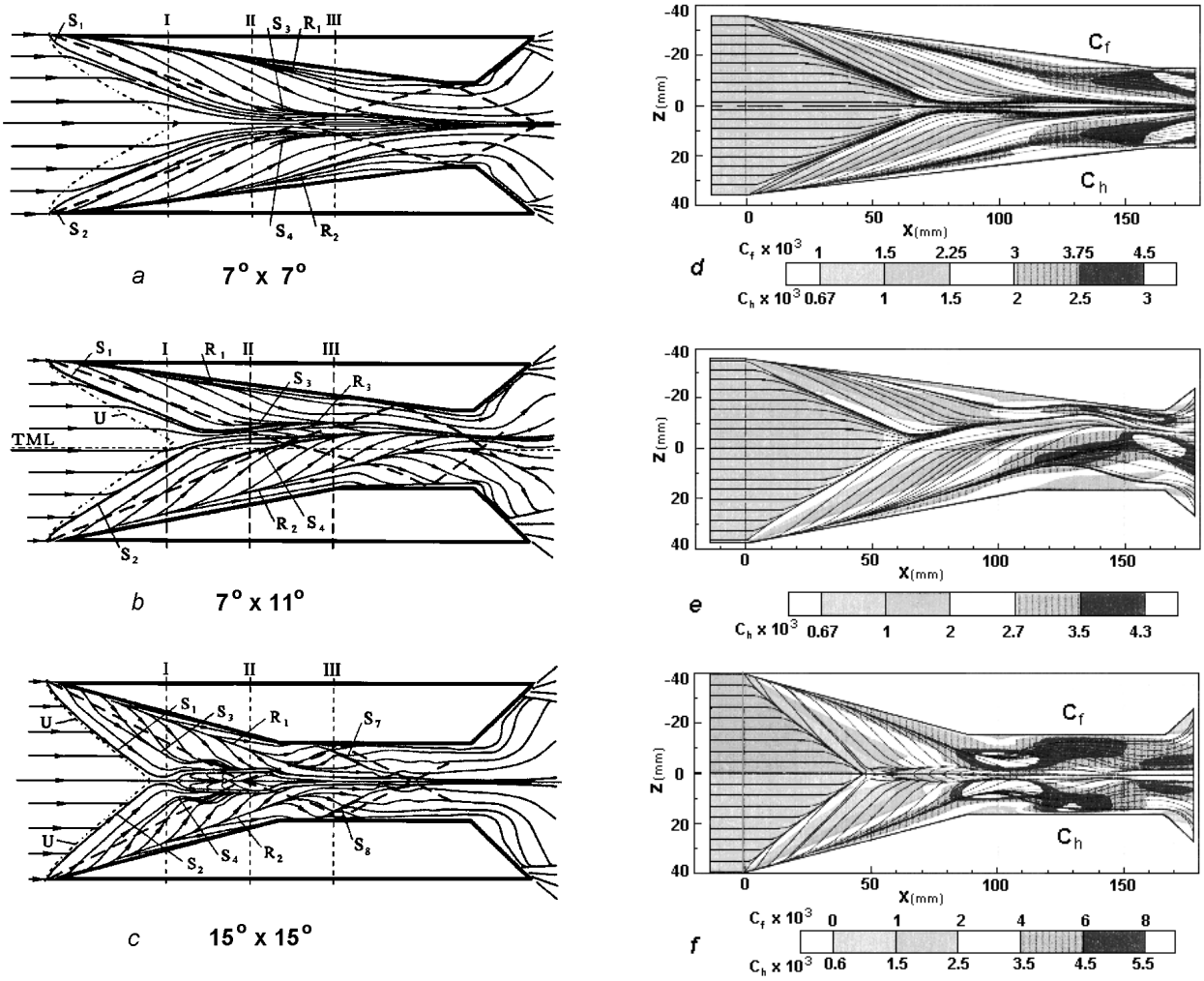

Fig. 2. Experimental topological schemes (*a–c*, from [4, 5]) and computed skin-friction/heat-transfer coefficients on the bottom wall (*d-f*, from [12, 13], with permission) at $M_\infty = 4$

of the grids. In the symmetrical cases (7°×7° weak interaction and 15°×15° strong interaction), the distributions of the skin-friction and heat-transfer coefficients are displayed in the upper part and lower part of the frames respectively; in the asymmetric case (7°×11° weak interaction), only the heat transfer coefficient is provided. The results are primary discussed in [12–14]. Our conclusion is that the surface flow pattern are at least comparable to and, at some points, slightly better than given by k–ε model and shown in [7–10]. The limiting streamlines on the plate in the experiments are smoothly deviated towards the channel axis along the shock traces corresponding to inviscid part of the flow (dashed lines in Figs. 2, *a–c*). These lines initially converge to the coalescence (or separation) lines S_1 and S_2. The upstream influence lines (indicated by the dash-dotted lines and marked *U*) denote the beginning of the rise in the surface pressure; they merge at or near the TML. Downstream, the lines S_1 and S_2 converge to form a characteristic throat. The more the interaction strengthens, the more the fluidic throat forms upstream and narrows. In the computations, the same features are evidenced in the weak interactions. In the 15°×15° case however, the computation predict a full separation of the incoming boundary layer and therefore, no fluidic throat. Similar features are typical for the computations with the k–ε model [5–10]. This is not in agreement with the experiment, where the fluidic throat still exists, and where the singular saddle point is located further downstream.

The secondary convergence (or separation) lines S_3 and S_4 are predicted in the weak and mild interaction cases (Fig. 2*, a, b, d, e*) and, in the asymmetric 7°×11° case, only on the 11° fin side. In the 15°×15° strong case, the experiment shows a strong convergence to these secondary separation lines (Fig. 2, *c*). A large-scale central separation region is formed behind the saddle point downstream the throat bounded by two additional coalescence lines which penetrates from the saddle point. The secondary separation lines S_3 and S_4 are close to merge with these coalescence lines approximately in the middle of the central separation zone. The computed topology is somewhat different (Fig. 2, *f*): it does not reveal the distinct secondary separation lines and demonstrates an appearance of the node point in the apex

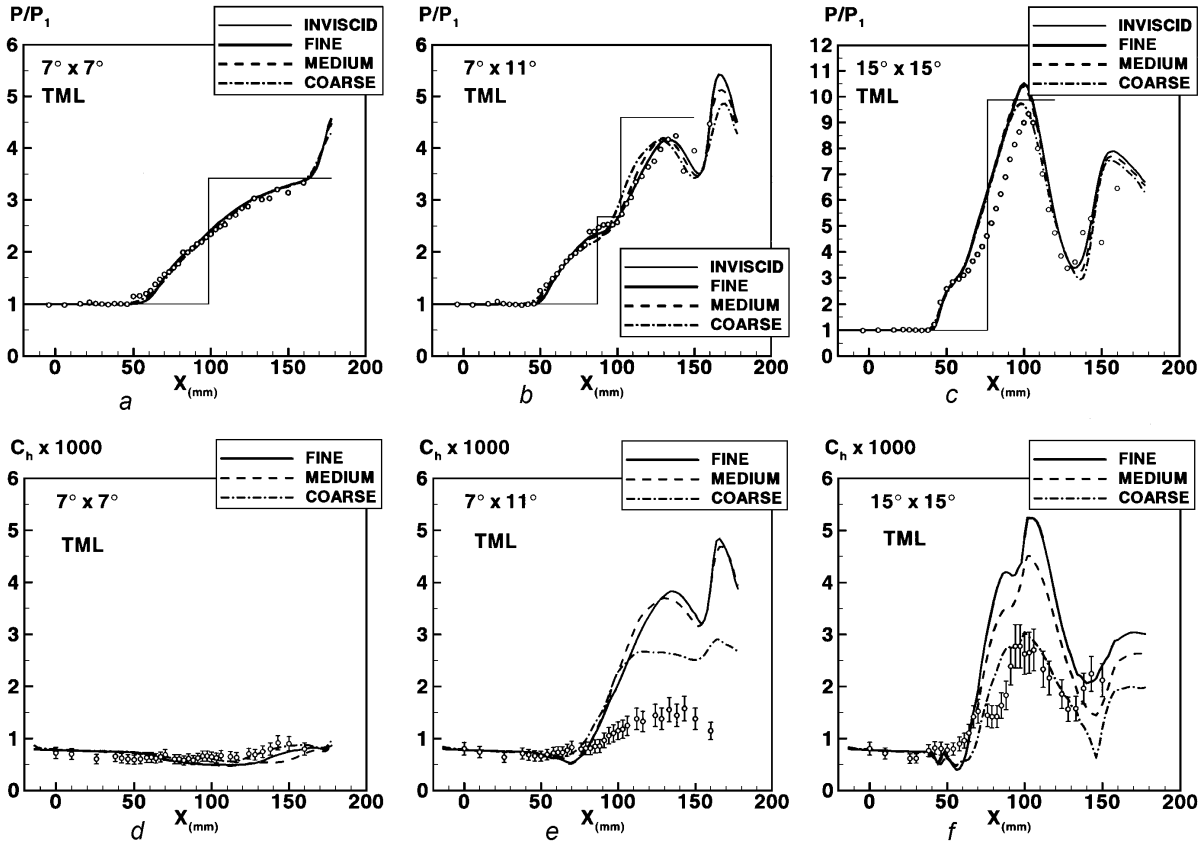

Fig. 3. Static pressure (*a–c*) and Stanton number (*d–f*) along the Throat Middle Line at $M_\infty = 4$ (from [13], with permission)

of the central separation zone [12–14]. The disappearance of the secondary separation lines in the computations may be related to a disagreement in the turbulence level in the near-wall region. Such a statement is supported by conclusions of the paper [27] and by previous experiments by Zheltovodov and Schülein [28, 29], with sand-grain roughness mounted in the secondary flow region, between the divergence and convergence lines of the one-fin configuration. By such way, they demonstrated that the secondary separation could be suppressed for weak and some mild interactions by initiating (or amplifying) turbulence in the separated flow.

The high heat fluxes are associated with the attachment of the Entrainment Flow (EF) which comes from an essentially inviscid part of the incoming flow, impinges the bottom wall along attachment lines R_1 and R_2 (Fig. 2) and then spreads out from these lines [11–14]. These attachment lines are clearly visible both in the computations and the experiments, and they compare very well to each other.

The mesh-convergence is verified for the pressure, adiabatic temperature, skin-friction and heat-transfer coefficients using the mesh-convergence index [12–14]. In the 7°×7° case, the pressure and C_h along the TML with the fine-grid solution is mesh-converged (Fig. 3, *a, d*). In the 7°×11° case (Fig. 3, *b, e*), it is concluded that the fine-grid solution is very close to the mesh-converged solution. In the 15°×15° configuration, the fine-grid may be compared with confidence with experimental data (Fig. 3, *c, f*). Note that the heat-transfer coefficient obtained on the coarse grid in the 15°×15° case compares very well to the experimental data (Fig. 3, *f*). Of course, this occurs only by chance and has no particular meaning. It is nevertheless interesting as an illustration of how wrong conclusions can be drawn from solutions which are not mesh-converged.

The comparison of computations on the basis of k–ε model for 7°×15° strong asymmetric interaction at $M_\infty = 4$ [10, 21, 22] is presented in Fig. 4. The computations distinctly reproduce the two primary separation lines S_1 and S_2 and divergence lines R_1, R_2, R_3. Nevertheless, the secondary separation line S_3 is suppressed in the computation (Fig. 4, *b*) comparing with experiment (Fig. 4, *a*). The upstream propagation of the line S_4 is also smaller in the computations than in experiment. In the cases with the k–ω this is related to a disagreement in the turbulence level in the near-wall region. The prediction of surface pressure distribution is rather good for this case (Fig. 4, *c, d*). An attempt was made to inhibit the transition of the fins sidewall boundary layer by limiting the production of turbulent kinetic energy in a k–ε model [9, 22]; it resulted in a rectification of the discrepancies between the flowfield visualization and simulations

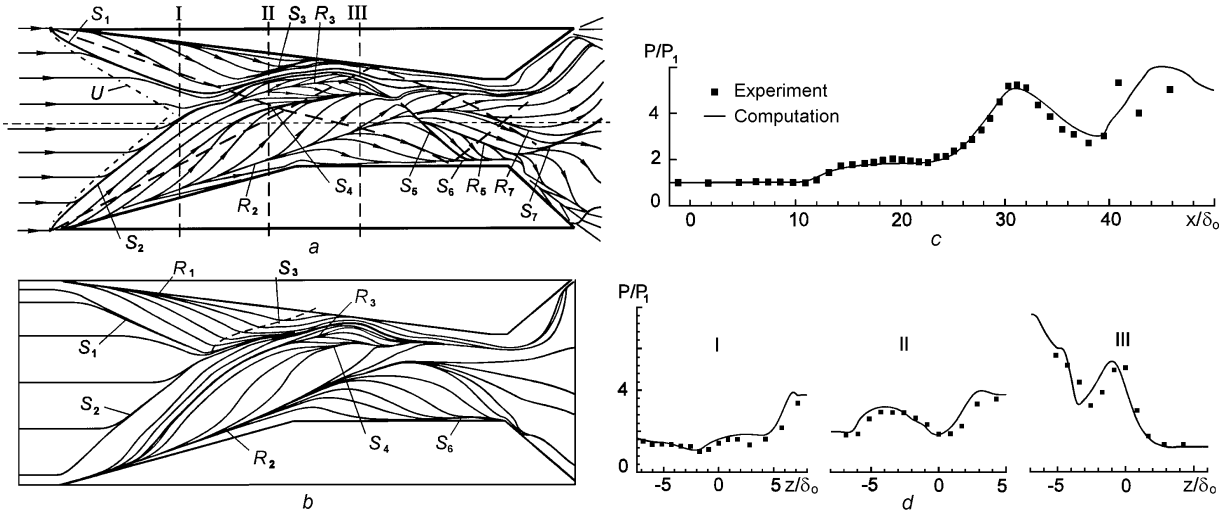

Fig. 4. Comparison of computations with experiment for 7°×11° case: oil-flow visualization (*a*), computed skin-friction lines (*b*), surface pressure along the TML (*c*) and cross sections I, II and III (*d*) at $M_\infty = 4$

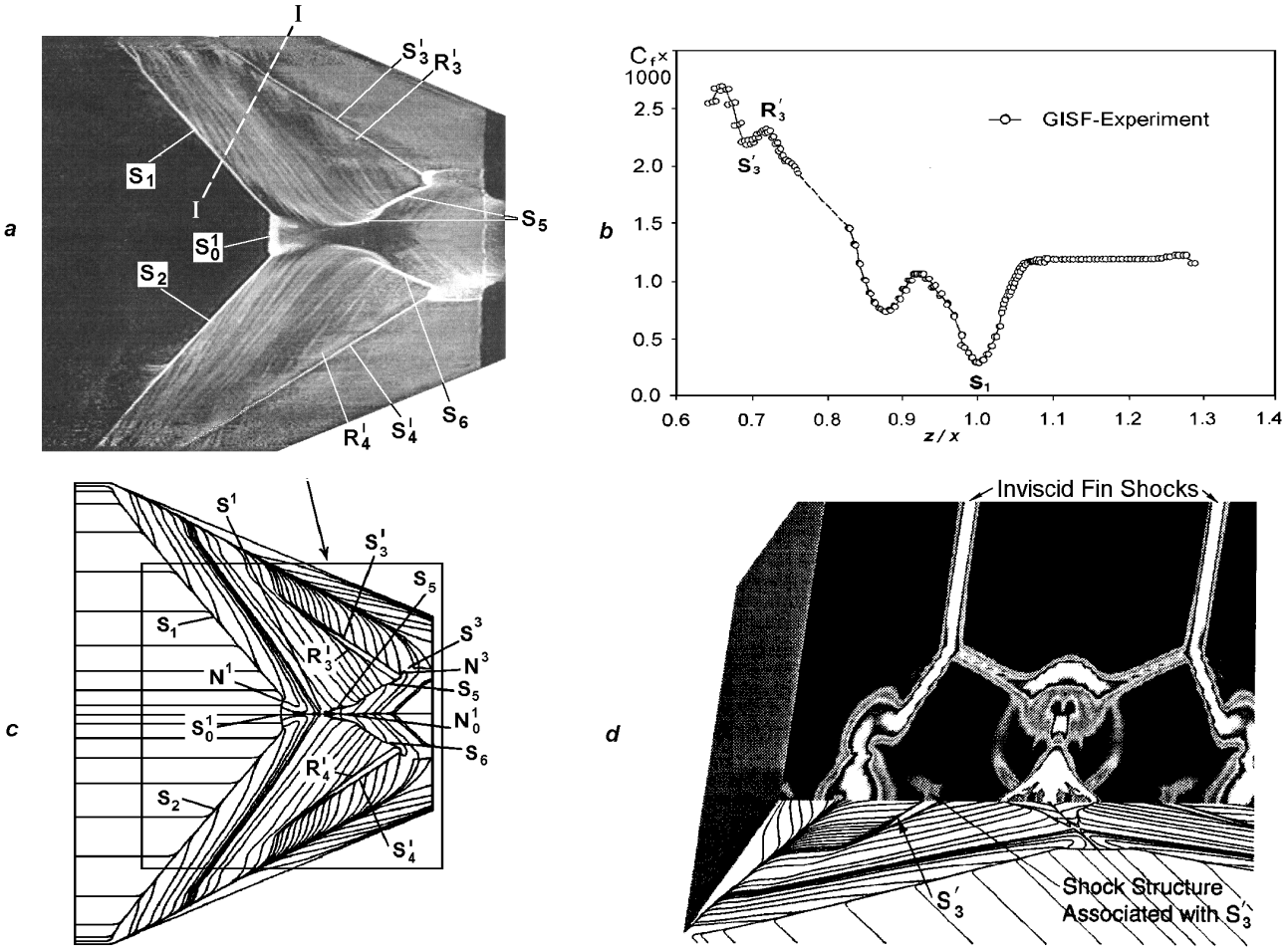

Fig. 5. Experimental and computational data for 23°×23° interaction at $M_\infty = 5$: oil-flow visualization (*a*, from [7, 16]), C_f measurements in section I (*b*), computed surface stream lines and shock waves (pressure gradient) structure (*c*, *d* – from [9, 23], with permission)

in the sidewall/shock-vortex interaction region. However, these modifications have no significant impact on the plate surface pattern.

The computations with standard k–ε model for the strongest 23°×23° interaction case at M_∞ = 5 [7, 9, 23] reproduce accurately main topological features revealed in the experiment (Fig. 5). In accordance with the analysis of the shock-wave/boundary-layer interaction regimes for one-fin configuration, presented in [27–29], the secondary separation and attachment lines S'_3, S''_4, R'_3, R''_4 (Fig. 5, *a*) appear in the near-wall supersonic turbulent cross flow in the vicinity of additional local normal shock waves at such conditions. The strength of such shocks is sufficient for stimulation of the secondary separation in the turbulent near wall flow. Strong variation of the surface skin friction coefficient in the interaction region (presented in the region of the quasi-conical flow, Fig. 5, *a*, section I) is illustrated on a basis of GISF measurements [15–17] (Fig. 5, *b*) with the using algorithm for the data processing developed by Schülein [17]. The computations reproduce very well the surface flow pattern (Fig. 5, *c*) and an appearance of local shock structure in the vicinity of secondary separation (Fig. 5, *d*) supporting experimental conclusion concerning a possibility of secondary separation of the turbulent near-wall flow. The comparison of the measured and computed spanwise pressure distribution with different meshes (see Table 2) demonstrate in general good agreement (Fig. 6). Nevertheless, significant discrepancy exists on the interaction centerline ($Z = z/\delta_0 = 0$) as in the considered above 15°×15° case (see Fig. 3, *c*). The spanwise pressure distribution also appears to be grid dependent in the region of the pressure rise approaching the fin face. The attempts to decrease the overprediction of surface pressure through limits on the production of turbulent kinetic energy in the 23°×23° case have not been fruitful [9]. Note that high level of CSW unsteadiness at such conditions [7] may be additional reason which stimulates discrepancy in surface pressure.

The regions of high levels of heat flux and skin friction as was indicated above have been found to correspond to the attachment lines of the 3-D flow originating from the upper part of the incoming boundary layer, or even the inviscid part of the flow [11, 14]. This flow crosses the primary shock waves before plunging down to the bottom wall. One hypothesis put forward in the literature [30] is that two-equation turbulence models predict a too large increase in the turbulent Kinetic Energy (TKE) in the outer part of the boundary layer across the shock waves, and that this excessive TKE is convected down to the wall due to the strong vortices formed behind shocks. The basis of this analysis is the mathematical concept of realizability [31, 32]: the variances of the fluctuating velocity components must be positive and the cross-correlations bounded by the Schwartz inequality. The goal of the studies [11, 12, 14] was to determine if the SWTBLI heat-flux issue was related to some violation of the realizability constraints.

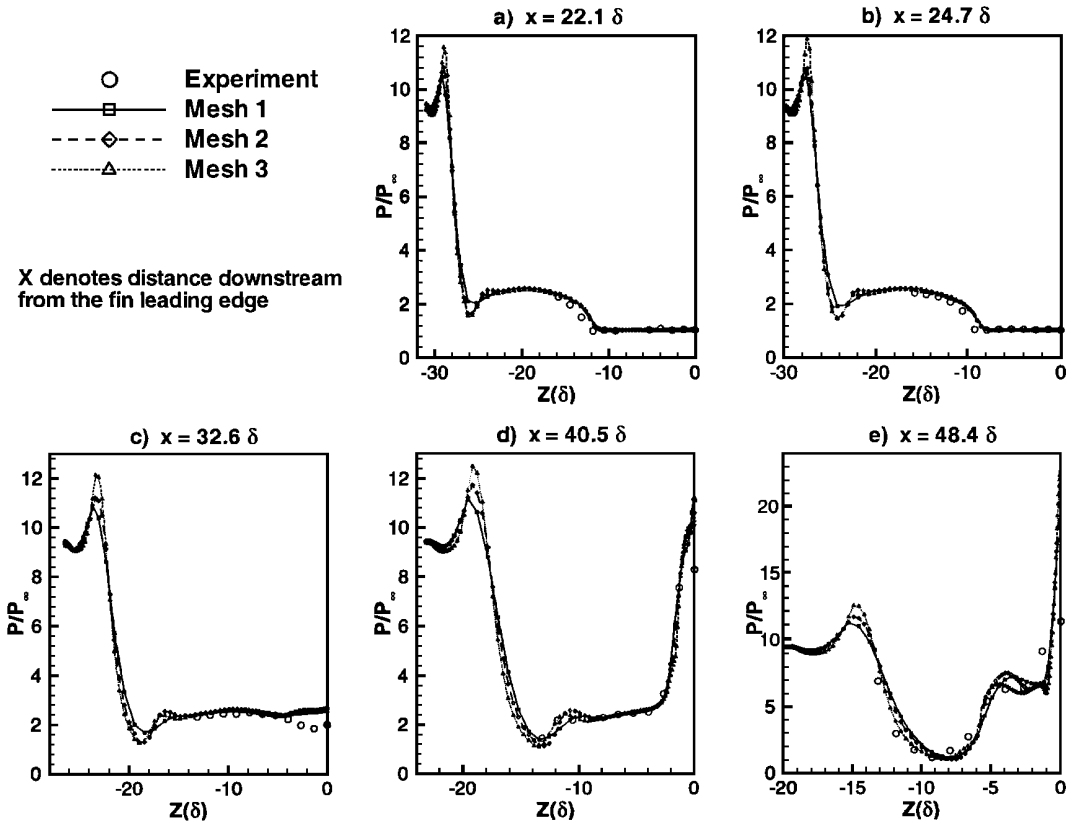

Fig. 6. Surface pressure distributions for 23°×23° interaction at M_∞ = 5 (from [7, 9], with permission)

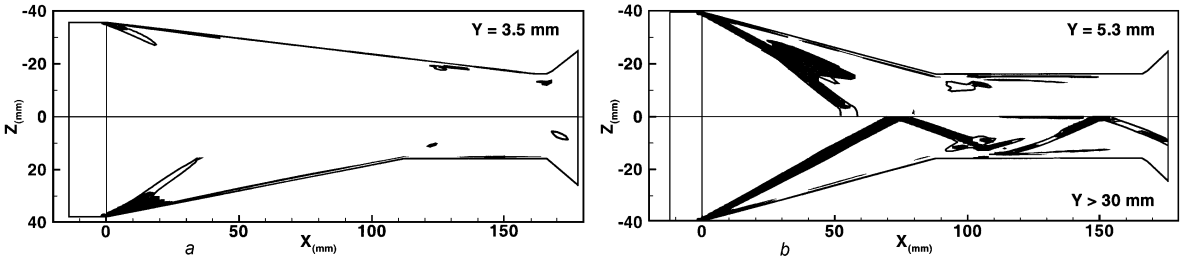

Fig. 7. Regions of violation of realizability constraints (gray zones) at $M_\infty = 4$: 7°×11° (*a*), 15°×15° (*b*) (from [14], with permission)

The solutions obtained with basic Wilcox's k–ω model are not realizable in the outer part of the boundary layer and above. In the 7°×11° configuration, in the section $y = \delta_0$, the realizability constraints are violated within the foot of the primary shock waves (Fig. 7, *a*); the irrealizable zone is larger on the 11° fin side than on 7° side. Another irrealizable zone is very narrow and extends parallel to the fin, not far from the location of the primary attachment line. In the 15°×15° configuration, the irrealizable zone is even larger and occupies the whole upper part of the lambda foot of the primary shock waves (Fig. 7, *b*, top). In the region of the flow not influenced by the bottom wall boundary layer (above y = 30 mm), the realizability constraints are violated across the shock wave only (Fig. 7, *b*, bottom part) with certainly no significant impact on the flow in the vicinity of the bottom wall. In the weak interaction case (7°×7°, not displayed here), no significant irrealizable zone is fixed outside the vicinity of inviscid shock waves [12]. The circled regions in the figures should contain the irrealizable zones in an incompressible flow in accordance with approach by Durbin [33].

A recent review of the realizability corrections to two-equation turbulence models [34] recalls that the idea is to enforced the realizability constrained by limiting the value of the constant α_v in the definition of the eddy viscosity $\mu_t = \alpha_v c_\mu \rho k/\omega$ (where $\omega = \varepsilon/k$). In order to determine the impact of the realizability enforcement on SWTBLI, four models have been tested [11, 12, 14]: so-called Wilcox – Moore (WM) and Wilcox – Durbin (WD) models (the realizability factor is used in accordance with [11, 14] to compute the eddy viscosity with the Moore and Moore [34] and Durbin [33] coefficients respectively). The versions in which the production term in the specific dissipation equation is kept at its original and maximum level are denoted WM^+ and WD^+ respectively.

In the 7°×11° configuration the pressure distribution is essentially unchanged by realizability corrections (Fig. 8, *a*) but the variation in the heat transfer predicting is seen (Fig. 8, *a, b*). Different considered turbulence models (WM, WD, WM^+ and WD^+) obtained some improvement of predicted C_h level but it is still high above the sparse experimental data and is close to predictions on the basis of different modifications of the k–ε model and Reynolds Stress Equations (RSE) considered in [6]. In the 15°×15° configuration, the realizability correction induce significant changes in the pressure distribution (Fig. 8, *c*) in some regions of the interaction zone. The evolution of the Stanton number is closely related to some changes in the topology of flow comparing to experiment which discussed in [11, 12, 14]. The streamlines arriving near the wall in the regions of overpredicted heat-transfer coefficients are shown to originate from very narrow regions close the fin leading edges, in the upper part of the incoming boundary layer, and to be associated with an increase of TKE when approaching the bottom wall, rather when crossing the shock waves. The realizability correction does not modify the computed topology, so that the features of C_h remains the same. Nevertheless, the levels

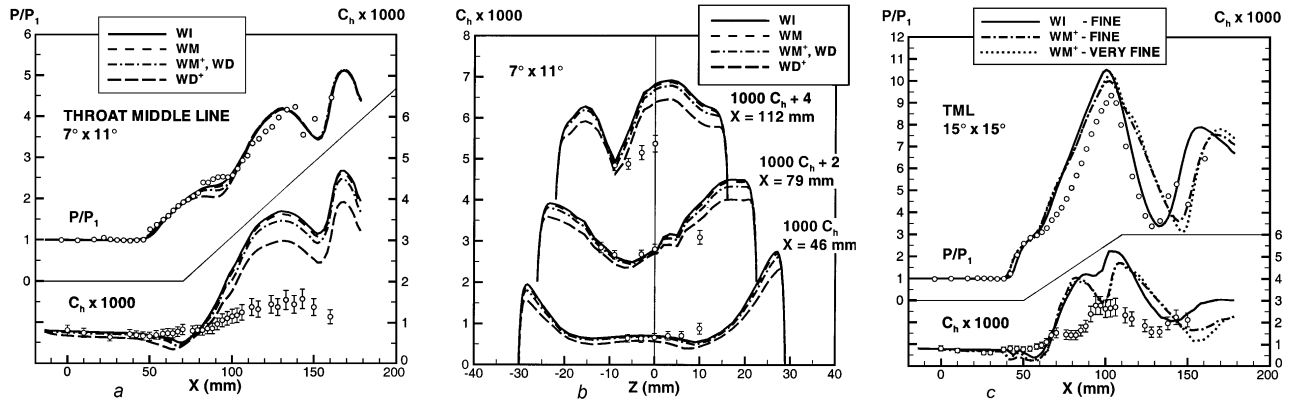

Fig. 8. 7°×11° medium grid pressure and heat transfer coefficient along the TML (*a*) and spanwise (*b*), 15°×15° – pressure and heat transfer coefficient along the TML for different grids (*c*) at $M_\infty = 4$ (from [14], with permission)

are significantly modified, essentially because of the lower turbulence level in the WM^+ solution. In the 7°×7° weak interaction case the pressure and the skin friction and heat transfer coefficients are lowered by at most 5 % in the interaction zone. It demonstrates that the modifications are not active in the case when the results are already quite good.

4. Conclusions

A systematic comparison of experimental and computational results has been considered in the cases of symmetric and asymmetric CSWTBLI at the Mach numbers $M_\infty = 4$ and 5. The topological features of such flows, surface pressure and heat transfer distributions in the interaction regions and the CSW structure have been examined in great detail. Experiment and computations with different modifications of k–ω and k–ε turbulence models agree on a lot of main features at various stages of the flows development. The topological features, as well as pressure distribution, are in close agreement in the week interaction case. Moderate to significant discrepancies occur in the mild and strong interactions in topology predicting on the stages of the central separated zone and secondary separation appearance and development. Nevertheless, they are successfully predicted for very strong interaction case. The pressure is always correctly predicted, except near the centerline and in the regions of primary attachment, where it is overestimated in the mild, strong and very strong interaction cases. It is demonstrated that the stronger the interaction, the more the numerical solutions violate the realizability principle and the heat flux prediction is sensitive to the realizability correction. Next stage of study is necessary to find a rational way for decreasing of the heat transfer overestimation for mild and strong interaction cases. The primary origin of the discrepancies between experiments and computations may be the turbulence level in the secondary flow: it seems to be much lower in the experiments than in computations. The unsteady nature of turbulent separation might also explain some discrepancies evidenced in the vicinity of singular separation points and the secondary separation lines.

Acknowledgements. The authors affiliated with ITAM were supported by the Russian Foundation for Basic Research (project code 97–01–00885) and the European Office of Aerospace Research and Development (EOARD grants No. F61708-970W0136 and F61775-98-WE091 monitored by Dr. C. Raffoul). Some of the experimental investigations were performed at the DLR Institute of Fluid Mechanics during a visit of the first author as Visiting Scientist and supported by the German Research Association (DFG Grant no. 436 RUS 17/29/97). The author affiliated with ONERA was supported by the French Delegation Generale pour l'Armement, Direction des Systemes de forces et de la Prospective, under Grants ERE No. 981075 and 9960053. The work was also supported in part by DGA/DSA/SPAe under Grant No. 90-95-005 BC-80. The computational resources were provided by NSF at the National Center for Supercomputing Applications, University of Illinois at Urbana-Champaighn under Grant No. MSS99 0001N. The numerical simulations of authors affiliated with Air Force Research Laboratory Wright-Patterson AFB were sponsored by AFOSR under tasks monitored by R. Canfield and S. Walker as well as in part by a grant of HPC time from the DoD HPC Shared Resource Center at CEWES and NAVO. The authors acknowledge several insightful communications with J. Shang and M. Visbal.

References

[1] Zheltovodov A.A. Shock waves/turbulent boundary-layer interactions – fundamental studies and applications // AIAA Paper 96-1977, 1996.

[2] Knight D.D. Numerical simulation of compressible turbulent flows using the Reynolds-averaged Navier – Stokes Equations // Turbulence in Compressible Flows, Advisory Group for Aerospace Research and Development, June 1997, AGARD Report, No. 819, P. 5-1 – 5-52.

[3] Knight D.D., Degrez G. Shock wave boundary layer interaction in high Mach number flows. A critical survey of Current CFD prediction capabilities // Hypersonic Experimental and Computational Capability, Improvement and Validation, Advisory Group for Aerospace Research and Development: AGARD Report. December 1998. No. 319. Vol. II. P. 1-1 – 1-35.

[4] Zheltovodov A.A., Maksimov A.I., Shevchenko A.M. Topology of three-dimensional separation under the conditions of symmetric interaction of crossing shocks and expansion waves with turbulent boundary layer // Thermophys. and Aeromech. 1998. Vol. 5, No. 3. P. 293–312.

[5] Zheltovodov A.A., Maksimov A.I., Shevchenko A.M., Knight D.D. Topology of three-dimensional separation under the conditions of asymmetrical interaction of crossing shocks and expansion waves with turbulent boundary layer // Thermophys. and Aeromech. 1998. Vol. 5, No. 4. P. 483–503.

[6] Knight D., Gnedin M., Becht R., Zheltovodov A. Numerical simulation of crossing-shock-wave/turbulent-boundary-layer interaction using a two-equation model of turbulence // J. Fluid Mech., 2000. Vol. 409. P. 121–147.

[7] Zheltovodov A.A., Maksimov A.I., Schülein E., Gaitonde D.V., Schmisseur J.D. Verification of crossing-shock-wave/boundary layer interaction computations with the k–ε turbulence model // Intern. Conf. on the Methods of Aerophys. Research: Proc. Pt. 1. Novosibirsk, Russia 9 – 16 July 2000. Novosibirsk, 2000. P. 231–241.

[8] Zheltovodov A.A., Maksimov A.I., Gaitonde D., Visbal M., Shang J.S. Experimental and numerical study of symmetric interaction of crossing shocks and expansion waves with a turbulent boundary layer // Thermophys. and Aeromech. 2000. Vol. 7, No 2. P. 155–171.

[9] Schmisseur J.D., Gaitonde D.V., Zheltovodov A.A. Exploration of 3-D shock turbulent boundary layer interactions through combined experimental/computational analysis. AIAA 2000–2378. 11 p.

[10] Gaitonde D., Shang J.S., Garrison T.J., Zheltovodov A.A., Maksimov A.I. Three-dimensional turbulent interactions caused by asymmetric crossing-shock configurations // AIAA J. 1999. Vol. 37, No.12. P.1602-1608.

[11] Thivet F., Knight D.D., Zheltovodov A.A. Computation of crossing-shock-wave/boundary-layer interactions with realizable two-equation turbulence models // Int. Conf. on the Methods of Aerophys. Research: Proc. Pt. 1. Novosibirsk, Russia, 9 – 16 July 2000. Novosibirsk, 2000. P. 195–201.

[12] Thivet F., Knight D.D., Zheltovodov A.A., Maksimov A.I. Some insights in turbulence modeling for crossing-shock-wave/boundary-layer interactions. AIAA 2000–0131. 16 p.

[13] Thivet F., Knight D.D., Zheltovodov A.A., Maksimov A.I. Numerical prediction of heat-transfer in supersonic inlets // Proc.: European Congress on Computational Methods in Applied Sciences and Engineering (ECCOMAS 2000), Barcelona, 11–14 September 2000, CD Contents. 21 p.

[14] Thivet F., Knight D.D., Zheltovodov A.A., Maksimov A.I. Insights in turbulence modeling for crossing-shock-wave/boundary-layer interactions // AIAA J., 2001. Vol. 39, No. 7.

[15] Schülein E., Zheltovodov A.A. Development of experimental methods for the hypersonic flows studies in Ludwieg tube // Intern. Conf. on the Methods of Aerophys. Research: Proc. Pt I. Novosibirsk, Russia, 29 June – 3 July, 1998. Novosibirsk, 1998. P. 191–199.

[16] Schülein E., Zheltovodov A.A. Documentation of experimental data for hypersonic 3-D shock waves / turbulent boundary layer interaction flows. DLR IB 223-99 A 26, Göttingen, 2001, 85 p.

[17] Schülein E. Skin friction and heat flux measurements in some 3-D supersonic turbulent separated flows (Messungen der Wandschubspannung und des Wärmeflusses in einigen turbulenten Strömungen mit Ablösungen im Überschall) // DLR IB 223 – 01 A 06, Göttingen, 2001 (to be published).

[18] Wilcox D.C. Reassessment of the scale-determining equation for advanced turbulence models // AIAA J., 1988. Vol. 26, No. 11. P.1299–1310.

[19] AeroSoft, Inc. *GASP*, General Aerodynamic Simulation Program Version 3. User's manual, May 1996.

[20] Wilcox D.C. Turbulence modeling for CFD. DCW Industries, Inc., La Canada, California, July 1998. 460 p.

[21] Gaitonde D., Shang J.S., Garrison T.J., Zheltovodov A.A., Maksimov A.I. Evolution of the separated flowfield in a 3-D shock wave/turbulent boundary layer interaction. AIAA 97-1837, June 1997. 14 p.

[22] Gaitonde D.V., Visbal M.R., Shang J.S., Zheltovodov A.A., Maksimov A.I. Parametric study of flowfield structure and validation issues in 3-D crossing-shock wave / turbulent boundary layer interactions // Intern. Conf. on the Methods of Aerophys. Research: Proc. Pt. 1. Novosibirsk, Russia 29 June – 3 July 1998. Novosibirsk, 1998. P. 67–80.

[23] Schmisseur J.D., Gaitonde D.V. Numerical investigation of new topologies in strong crossing shock-wave / turbulent boundary layer interactions. AIAA 2000–0931. 13 p.

[24] Beam R., Warming R. An implicit factored scheme for the compressible Navier – Stokes equations // AIAA J. 1978. Vol.16, No. 4. P. 393–402.

[25] Jones W.P., Launder B.E. The prediction of laminarization with a two-equation model of turbulence. Intern. J. of Heat and Mass Transf. 1972. No.15. P. 301–314.

[26] Launder B.E., Sharma A.I. Application of the energy dissipation model of turbulence to the calculation of flows near a spinning disk // Letters in Heat and Mass Transfer. 1974. No. 1. P.131–138.

[27] Zheltovodov A.A. Regimes and properties of 3D separated flows initiated by swept shock waves // J. Appl. Mech. Techn. Phys. 1982. No. 3. P. 116–123.

[28] Zheltovodov A.A., Pavlov A.A., Schülein E., Yakovlev V.N. Interconnectionship between the flow separation and direct and inverse transition at supersonic speed conditions. IUTAM Symp. on Laminar-Turbulent Transition, Novosibirsk, USSR, July 1984 / Ed. by V.V.Kozlov, Berlin, Springer Verlag, Heidelberg, 1985. P. 503–508.

[29] Zheltovodov A.A., Maksimov A.I., Schülein E. Development of turbulent separated flows in the vicinity of swept shock waves // The Interactions of Complex 3-D Flows. Novosibirsk: ITAM USSR Acad. Sci., Siberian Branch, 1987. P. 67-91 (in Russian).

[30] Knight D.D. Simulation of shock wave-turbulent boundary layer interactions using the Reynolds-averaged Navier – Stokes equations // Modeling Complex Turbulent Flows: ICASE/LaRC/AFOSR Symposium, Hampton, Virginia, Aug. 1977 / Eds. M.D. Salas, J.N. Hefner, and L. Sakell, ICASE/LaRC Interdisciplinary Series in Science and Engineering, Vol. 7. Dordrecht: Kluwer Academic Publisher, 1999. P. 276–296.

[31] Schumann U. Realizability of Reynolds stress turbulence models // Phys. Fluids. 1977. Vol. 20. P. 721–725.

[32] Lumley J.L. Computational modeling of turbulent flows // Advances in Applied Mechanics. Academic Press, 1978, Vol. 18. P. 123–176.

[33] Durbin P.A. On the k–ε stagnation point anomaly // Intern. J. Heat & Fluid Flow. 1996. Vol. 17, No. 1. P. 89–90.

[34] Moore J.G., Moore J. Realizability in two-equation turbulence models. AIAA Paper 99-3779, 1999.